

# Prediction of Release-Etch Times for Surface-Micromachined Structures

William P. Eaton\*,†, Robert L. Jarecki\*\*, and James H. Smith\*

\*Intelligent Micromachines Department, Mail Stop 1080

\*\*Sub-0.35  $\mu\text{m}$  Processes Department, Mail Stop 1077

Sandia National Laboratories, P.O. Box 5800, Albuquerque, NM 87185, USA

RECEIVED

MAY 08 1997

OSTI

## SUMMARY

A one-dimensional model is presented which describes the release-etch behavior of sacrificial oxides in aqueous HF. Starting from first principles and an empirical rate law, release etch kinetics are derived for primitive geometries. The behavior of complex three-dimensional structures is described by joining the solutions of constituent primitives and applying appropriate boundary conditions. The two fitting parameters,  $k_1$  and  $k_2$ , are determined from the simplest structure and describe the more complex structures well. Experimental validation of the model is presented with data for all of the geometries and four types of sacrificial oxides and.

## MOTIVATION

A common desire in surface-micromachining is to reduce the release-etch time. Unfortunately, linear etch rates do not apply to large lateral etch distances, since diffusion limitations are encountered. Hence, a more sophisticated method of determining etch times is required.

Release-etch modeling for surface-micromachining was first examined in detail by Monk *et al.*[1-7]. They examined effects of etchant concentration, etchant pH, etchant additives, and etch channel height and width effects on etching behavior. Liu *et al.*[8] and Tai *et al.*[9] added an empirical formulation of the etch kinetics. Like Monk *et al.*, they used rectangular etch channels exclusively (Figure 2a). In this paper, the above work is extended by adding more geometric complexity to the available models. The range of structures is shown in Figure 2 and 3.

## THEORY

Modeling of release etching in this work is based upon finding relationships among flux, concentration, and etch rate. Details of the model have been reported previously[10], and the method of solution is briefly discussed here. The basic equations of the model are given in Table 2, and the conventions are illustrated in Figure 1. The reader is referred to Table 1 for definitions of variables.

The oxide etch rate,  $\delta$ , is presumed to be directly proportional to the flux of HF to the etch front,  $J_{HF}$  (Equation 2). The proportionality constant is inferred from the net reaction of HF with  $\text{SiO}_2$  (Equation 1). The flux is determined from two sources: Fick's first law, and an empirical rate law,  $k_1C + k_2C^2$ . According to and Liu *et al.*[8] and Tai *et al.*[9], this is a good empirical choice

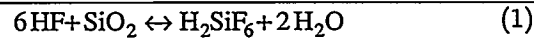
Table 1. List of variables. N geometries: P=port, B=bubble, C=concentric circles, PP=port-to-port, PB=port-to-bubble, BW=bubble-to-wedge, PBW=port-to-bubble-to-wedge.

variable	description
$a$	proportionality constant.
$A$	constant of integration.
$C(x)$ , $C(r)$	concentration of HF at position $x, r$ .
$C(\delta)$	concentration of HF at etch front.
$C_0$	bulk concentration of HF.
$\delta_N, h_N$	width, height of sac. oxide for geometry N.
$\delta$	position of etch front.
$\delta_{bw}$	radius above which wedge solution is valid.
$D$	diffusivity of HF in water.
$\phi$	angle determined by number of etch ports.
$\gamma_N$	geometrical constant for etching regime N.
$J_{HF}$	flux of HF to etch front.
$k_1, k_2$	first and second order rate constants.
$L$	length of etch port.
$MW_{SiO_2}$	molecular weight of $\text{SiO}_2$ .
$n$	number of etch ports for PBW geometry.
$\theta_N$	decreasing angle in wedge regime.
$\rho_{SiO_2}$	mass density of $\text{SiO}_2$ .
$r, x$	radial and linear coordinates.
$s$	hole-to-hole or 2x hole-to-wall spacing.
$t$	etch time.

for the kinetics of the reaction, since it describes etch behavior over a wide range of concentrations.

Both convective components and the instantaneous rate of change of the concentration are presumed to be small, so that Fick's second law is written as Equation 4. The concentration is  $C_0$  at  $x = 0$  or  $r_0$ , so that solving Equation 4 yields Equations 5 and 6 for linear and polar

Table 2. Theoretical foundations of release-etch model. Details are given in reference [10]



$$\frac{d\delta}{dt} = \alpha J_{HF}, \quad \alpha = \frac{1}{6} \frac{MW_{SiO_2}}{\rho_{SiO_2}} \quad (2)$$

$$J_{HF} = -D\nabla C = k_1C + k_2C^2 \quad (3)$$

$$\nabla^2 C = 0 \quad (4)$$

$$C(x) = Ax + C_0 \quad (5)$$

$$C(r) = A \ln\left(\frac{r}{r_0}\right) + C_0 \quad (6)$$

†Present address: Reliability Physics Department, Sandia National Laboratories, Albuquerque, NM 87185-1081, USA, w.p.eaton@ieee.org

MASTER

DISTRIBUTION OF THIS DOCUMENT IS UNLIMITED

IN

## **DISCLAIMER**

This report was prepared as an account of work sponsored by an agency of the United States Government. Neither the United States Government nor any agency thereof, nor any of their employees, makes any warranty, express or implied, or assumes any legal liability or responsibility for the accuracy, completeness, or usefulness of any information, apparatus, product, or process disclosed, or represents that its use would not infringe privately owned rights. Reference herein to any specific commercial product, process, or service by trade name, trademark, manufacturer, or otherwise does not necessarily constitute or imply its endorsement, recommendation, or favoring by the United States Government or any agency thereof. The views and opinions of authors expressed herein do not necessarily state or reflect those of the United States Government or any agency thereof.

## **DISCLAIMER**

**Portions of this document may be illegible  
in electronic image products. Images are  
produced from the best available original  
document.**

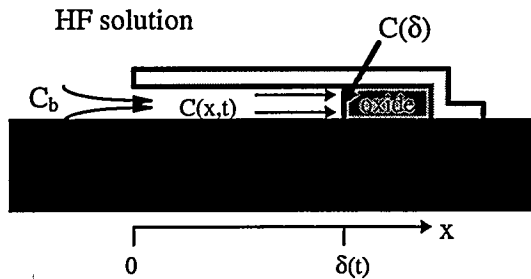


Figure 1. Conventions for coordinates and concentrations of release-etch model. After references REFS

symmetry, respectively.

In many cases solving etch front position as a function of time,  $\delta(t)$ , provides more insight than the etch rate,  $d\delta/dt$ , and therefore requires an integration. In all cases except for the rectangular etch port, numerical integrations must be used, and can be performed with commercial mathematical software, such as Mathematica™, Maple™, MathCAD™, or others. Furthermore, it is generally easier to solve for  $t(\delta)$  instead of  $\delta(t)$ , where the integration takes the form

$$t(\delta) = \int_{\xi}^{\delta} \frac{d\delta}{\alpha(k_1 C + k_2 C^2)}, \quad (7)$$

where  $x$  is  $0$ ,  $r_0$ ,  $\delta_{bp}$ , or  $R_0$ , depending on the geometry in question.

### Primitive Geometries

The three primitives considered are the rectangular etch port, bubble, and concentric circles. Completed test structures are shown in Figure 2. The relevant solutions to all of the concentrations and etch times are given in Table 3. The rectangular etch port (Figure 2a) is the simplest of all geometries and consists of a rectangular box that is open at one end to HF. The bubble geometry

Table 3. Solutions for primitives. The general form for etch times is given by Equation 7.

port
$C_p(\delta) = \frac{\sqrt{(k_1\delta + D)^2 + 4k_2\delta C_0 D} - (k_1 + 2k_2 C_0)\delta - D}{2k_2\delta}$
$t_p(\delta) = \frac{k_1[k_1(\delta + D) + 2k_2 C_0 D]\sqrt{(k_1\delta + D)^2 + 4k_2 C_0 D} + (k_1 + 2k_2 C_0)(k_1^2\delta - D^2) + 2k_1^2\delta D}{2k_2\delta} - \frac{k_2 D}{k_1^2} \ln\left(\frac{k_1\sqrt{(k_1\delta + D)^2 + 4k_2 C_0 D} + k_1^2[k_1(\delta + D) + 2k_2 C_0 D]}{2D(k_1 + 2k_2 C_0)}\right)$
bubble
$C_B(\delta) = \frac{\sqrt{\left(k_1\delta \ln\left(\frac{r}{r_0}\right) + D\right)^2 + 4k_2\delta \ln\left(\frac{r}{r_0}\right)C_0 D} - k_1\delta \ln\left(\frac{r}{r_0}\right)D - D}{2k_2\delta \ln\left(\frac{r}{r_0}\right)}$
concentric circles
$C_B(\delta) = \frac{\sqrt{\left(k_1\delta \ln\left(\frac{r}{r_0}\right) - D\right)^2 - 4k_2\delta \ln\left(\frac{r}{r_0}\right)C_0 D} - k_1\delta \ln\left(\frac{r}{r_0}\right)D + D}{2k_2\delta \ln\left(\frac{r}{r_0}\right)}$

(Figure 2b) is a circular or semicircular structure that is anchored at its edges and etched from an ~~etch~~ in its center. The concentric circles geometry (Figure 2c) is a circular structure that is anchored at its center and etched from its edges.

### Complex Geometries

Complex geometries are broken up into their primitive constituents. Fabricated test structures of all of the primitive geometries are shown in Figure 3. Additional total mass flux boundary conditions are required to join primitive solutions. For example, the boundary condition for the port-to-port structure (Figure 3a), which is two rectangular etch ports joined end to end, is

$$(J_{1^{st} port})(Area_{1^{st} port}) = (J_{2^{nd} port})(Area_{2^{nd} port}). \quad (8)$$

In this case the flux is said to change discontinuously when the etch proceeds into the second port. However, the other solutions can be easily forced to change continuously.

The port-to-bubble geometry (Figure 3b) is a rectangular etch port joined to a semicircular region. As the etch proceeds into the bubble regime, the etch front is an ever-expanding semicircle until all of the sacrificial oxide is consumed.

The bubble-to-wedge geometry (Figure 3c) is particularly useful, since it describes the etching of surface micromachined structures from a square array of etch holes. This is the configuration used for many devices, such as accelerometers and comb drives. The etch front starts out with a circular shape until it meets a wall or a neighboring etch front. Then the etch front is broken into four wedge-shaped regions. Because of the symmetry of the problem, only one wedge needs to be examined. An angle,  $\theta_{BW}$ , is constructed which accounts for the decreasing etch front area as the etch progresses. It starts at  $\pi/2$  and diminishes to zero.

The port-to-bubble-to-wedge (Figure 3c) geometry describes the etching of a large, regular-polygonal area from its edges. This type of structure has been used to make diaphragms for surface-micromachined pressure sensors and flow sensors. Because of the symmetry of the structure, only one etch port needs to be tracked through the release-etch. First the rectangular etch port is etched, then as the etch proceeds underneath the diaphragm, a "bubble" forms. Once all of the adjoining etch fronts collide the etch proceeds into the wedge regime with angle  $\theta_{PBW}$ .

### RESULTS

The etch structures of Figure 2 and 3 were made by depositing and patterning 1  $\mu\text{m}$  thick sacrificial oxides, followed by depositing and patterning 0.8  $\mu\text{m}$  of low stress silicon nitride. Four types of sacrificial oxide were used: undoped LPCVD oxide, 2.6 wt% boro-silicate glass (BSG), 2.4 wt% phospho-silicate glass, and 4.8 wt%/3.7 wt% boro-phospho-silicate glass (BPSG). Six inch silicon substrates with etch structures were diced into individual die. The ~~dice~~ were placed in individual baskets for the etch studies. At time zero, the etch tank was filled with

Table 4. Solutions for complex structures. Etch times are given in general by Equation 7.

	port-to-port	hole
$C_{PP}(\delta) = C_P(\delta) \Big _{C_0 \rightarrow C_{0PP}}, \quad \gamma_{PP} = \frac{d_{PP}h_{PP}}{d_P h_P} L,$		
$C_{0PP}(\delta) = \frac{2k_2 C_0 \delta^2 - \gamma_{pp} \left[ \sqrt{\left[ k_1(\delta + \gamma_{PP}) + D \right]^2 + 4k_2 C_0 D(\delta + \gamma_{PP})} + (k_1 - 2k_2 C_0) \delta + k_1 \gamma_{PP} + D \right]}{2k_2(\delta + \gamma_{PP})^2}$	port-to-bubble	hole
$C_{PB}(\delta) = C_B(\delta) \Big _{C_0 \rightarrow C_{0PB}}, \quad \gamma_{PB} = \frac{\pi h_{PB}}{d_P h_P},$		
$C_{0PB}(\delta) = \frac{2k_2 C_0 \delta \left[ \ln\left(\frac{\delta}{r_0}\right) \right]^2 - \gamma_{PB} \left[ (k_1 - 2k_2 C_0) \delta \ln\left(\frac{\delta}{r_0}\right) + k_1 \gamma_{PB} + D - \sqrt{\left[ k_1 \left( \delta \ln\left(\frac{\delta}{r_0}\right) + \gamma_{PB} \right) + D \right]^2 + 4k_2 C_0 D \left( \delta \ln\left(\frac{\delta}{r_0}\right) + \gamma_{PB} \right)} \right]}{2k_2 \delta \left[ \gamma_{PB} + \ln\left(\frac{\delta}{r_0}\right) \right]^2}$	bubble-to-wedge	hole
$C_{BW}(\delta) = C_B(\delta) \Big _{C_0 \rightarrow C_{0BW}}, \quad C_{0BW}(\delta) = C_{0PB}(\delta) \Big _{\gamma_{PB} \rightarrow \gamma_{BW}}, \quad \gamma_{BW} = \frac{2\theta_{BW}}{\pi} \ln\left(\frac{\eta}{\delta_{bp}}\right), \quad \theta_{BW} = \frac{\pi}{2} - \cos^{-1}\left(\frac{s}{2\delta}\right).$	port-to-bubble-to-wedge	hole
$C_{PBW}(\delta) = C_B(\delta) \Big _{C_0 \rightarrow C_{0PBW}}, \quad C_{0PBW}(\delta) = C_{0PB}(\delta) \Big _{\gamma_{PB} \rightarrow \gamma_{PBW}}, \quad \gamma_{PBW} = \frac{\theta_{PBW}}{\pi} \ln\left(\frac{r_0}{\delta_{bp}}\right),$ $\theta_{PBW} = 4 \tan^{-1} \left( \frac{\delta \cos\left(\frac{\phi}{2}\right) - \sqrt{\delta^2 - \frac{1}{4} \sin^2 \phi (R_0^2 + \delta_{bp}^2)}}{\sin\left(\frac{\phi}{2}\right) \left( \delta + \cos\left(\frac{\phi}{2}\right) \right) \sqrt{R_0^2 + \delta_{bp}^2}} \right), \quad \phi = \frac{2\pi}{n}, \quad C_\beta = \text{Root} \left\{ \left[ \gamma_{PBW} + \ln\left(\frac{\delta_{pb}}{r_0}\right) \right] C_{0PBW} - \left[ \gamma_{PBW} + \ln\left(\frac{\delta_{pb}}{r_0}\right) \right] C_\beta = 0, C_\beta \right\}.$		

49 wt% HF, thereby immersing the dice. Dice were then removed from the tank at regular intervals and the etch was quenched in deionized water. The quenched etch front positions were measured optically.

For all of the different oxides, the etch kinetics,  $k_1$  and  $k_2$  were determined from the simplest structures, the rectangular etch ports, using a nonlinear least-squares fit. These coefficients were then applied to the more complex solutions. Theoretical and experimental curves are shown in Figures XX and coefficients  $k_1$  and  $k_2$  are given in Table 5. A value of  $1.6 \cdot 10^{-5}$  [cm<sup>2</sup>/sec] was used for the diffusivity of HF in water.

Of all of the different oxides, the undoped LPVCD oxide results had the worst fit to theory. This was due in part to the fact that the etch front shapes of the undoped oxide films were notch-shaped for the rectangular etch ports. This notch-shape evolved during the course of the etch, making specifying the location of the etch front difficult. The shape was presumed to be due to unrelieved stresses in the sidewalls of the films, causing the edges to etch faster than the bulk. The other oxides had flat etch fronts and fit much better to the theoretical model.

Table 5. Etch kinetics for all four oxides used in paper.

Sacrificial Layer	$k_1$ [cm/sec]	$k_2$ [cm <sup>4</sup> /mole·sec]
undoped oxide	$3.0 \cdot 10^{-7}$	$3.1 \cdot 10^{-3}$
2.6% BSG	$4.5 \cdot 10^{-5}$	$7.0 \cdot 10^{-4}$
2.4% PSG	$1.1 \cdot 10^{-4}$	$4.6 \cdot 10^{-3}$
4.8/3.7 BPSG	$4.5 \cdot 10^{-4}$	$1.7 \cdot 10^{-2}$

## ACKNOWLEDGEMENTS

Special thanks go to the staff and operators of Sandia National Laboratories' Microelectronics Development Laboratory, without whom the test structures could not have been made.

Sandia is a multiprogram laboratory operated by Sandia Corporation, a Lockheed Martin Company, for the United States Department of Energy under contract under contract DE-AC04-94AL85000.

## REFERENCES

- [1] D. J. Monk, *Controlled Structure Release for Silicon Surface Micromachining*, Ph.D. Thesis, University of California at Berkeley, 1993.
- [2] D. J. Monk, D. S. Soan, and R. T. Howe, "Sacrificial layer SiO<sub>2</sub> wet etching for micromachining applications", *Digest of Technical Papers: Transducers 91*, pp. 647-650 (1991).
- [3] D. J. Monk, D. S. Soan, and R. T. Howe, "A diffusion/chemical reaction model for HF etching of LPCVD phosphosilicate glass sacrificial layers", *Technical Digest: IEEE Solid State Sensor and Actuator Workshop*, pp. 46-49 (1992).
- [4] D. J. Monk, D. S. Soan, and R. T. Howe, "Determination of the etching kinetics for the hydrofluoric acid/silicon dioxide system," *J. ECS*, 140(8), pp. 2339-2346 (Aug. 1993).
- [5] D. J. Monk, D. S. Soan, and R. T. Howe, "A review of the chemical reaction mechanism and kinetics for hydrofluoric acid etching of silicon dioxide for surface micromachining applications," *Thin Solid Films*, 232(1), pp. 1-12 (10 Sept. 1993).
- [6] D. J. Monk, D. S. Soan, and R. T. Howe, "Hydrofluoric

acid etching of silicon dioxide sacrificial layers, part I. Experimental observations," *J. ECS*, 141(1), pp. 264-269 (Jan. 1994).

[7] D. J. Monk, D. S. Soane, and R. T. Howe, "Hydrofluoric acid etching of silicon dioxide sacrificial layers, part II. Modeling," *J. ECS*, 141(1), pp. 270-274 (Jan. 1994).

[8] J. Liu, Y.-C. Tai, J. Lee, K.-C. Pong, Y. Zohar, and C.-H. Ho, "In Situ monitoring and universal modeling of sacrificial

PSG etching using hydrofluoric acid", *Proceedings of Micro Electro Mechanical Systems, IEEE*, pp. 71-76 (February 1993).

[9] Y.-C. Tai and C.-M. Ho, "Silicon Micromachining and Its Applications", *Proc. SPIE*, Vol 2448, pp. 141-151 (Mar. 1995).

[10] W. P. Eaton, R. L. Jarecki, and J. H. Smith, "Release-etch modeling for complex surface-micromachined structures", *Proc. SPIE*, Vol 2879, pp. 80-93 (Oct. 1996).

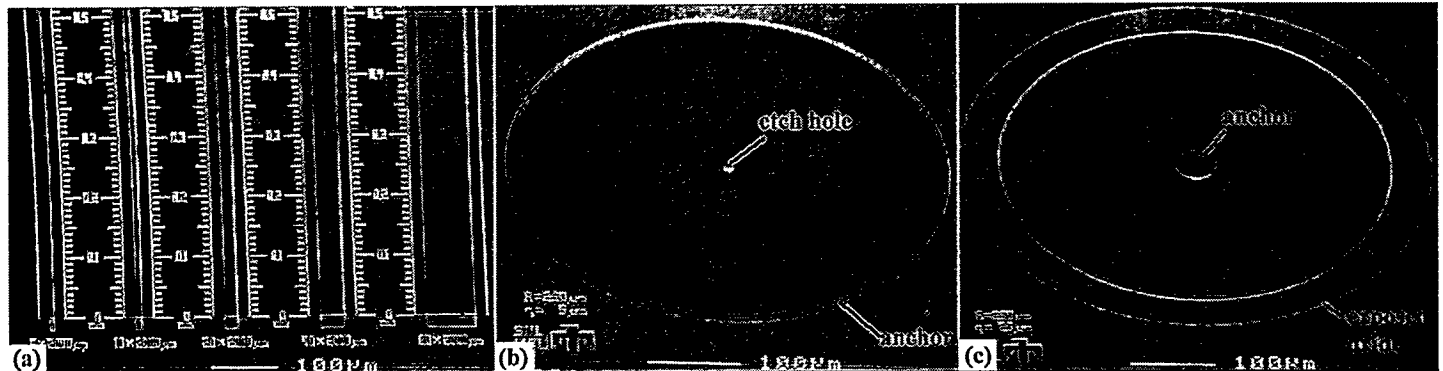


Figure 2. Scanning electron micrographs of fabricated primitives. (a) rectangular port. (b) bubble. (c). concentric circles.

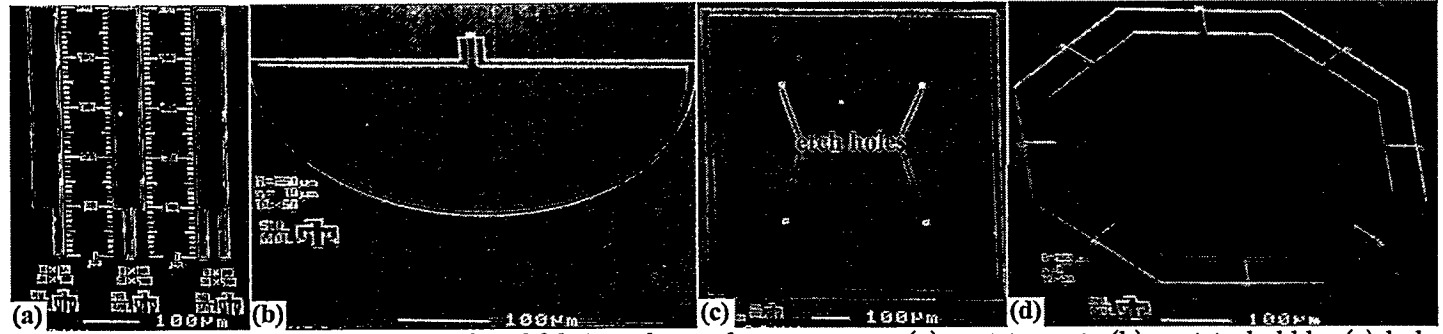


Figure 3. Scanning electron micrographs of fabricated complex structures. (a) port-to-port. (b) port-to-bubble. (c) bubble-to-wedge. (d) port-to-bubble-to-wedge.

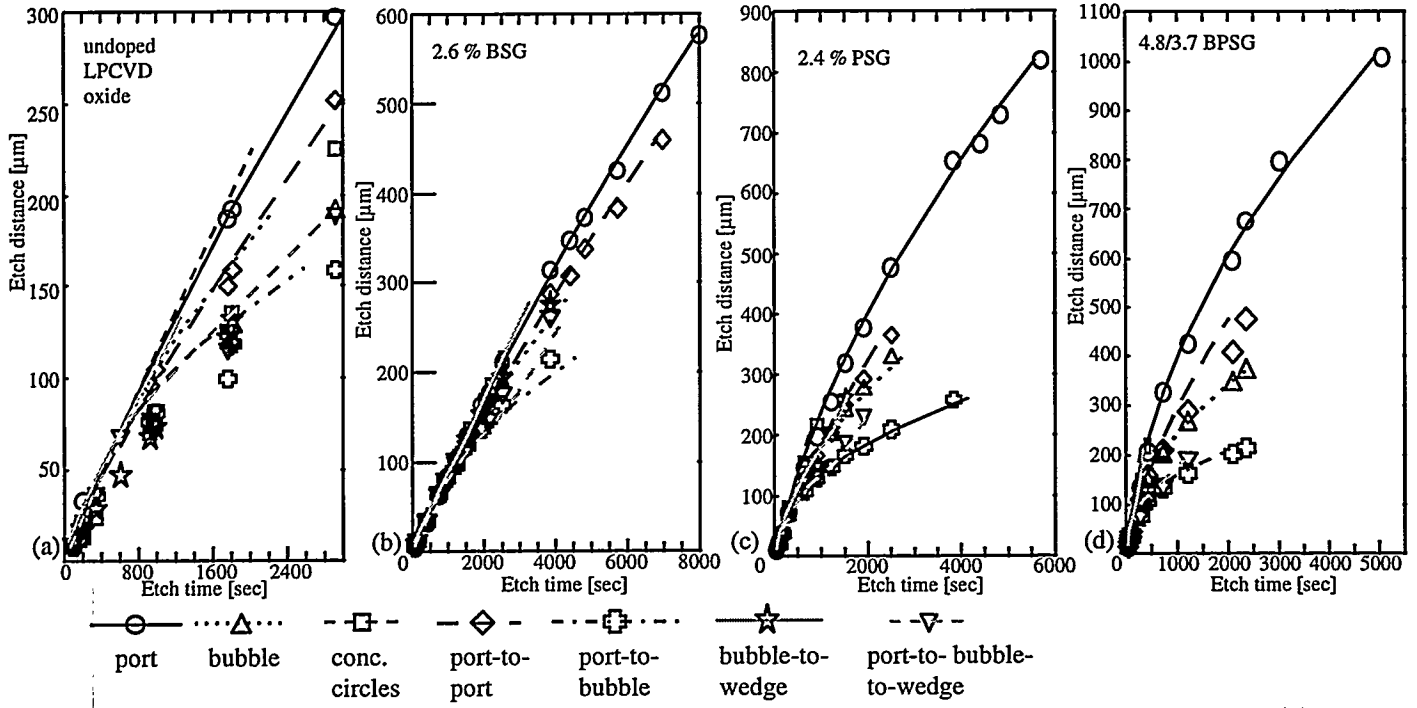


Figure 4. Etch distance [ $\mu\text{m}$ ] vs etch time[sec] for four different sacrificial oxides and all geometries. (a) undoped LPCVD oxide. (b) 2.6% BSG. (c) 2.4% PSG. (d) 4.8/3.7 BPSG.